

# Dissolution Manufacturing Strategy for Designing Efficient and Low Cost Polymeric Solar Water Evaporator

Wenqing Ruan, Heting Zhang, Jianan Fu,\* Zhen Li, Jinbiao Huang, Zehang Liu, Shenghao Zeng, Zhe Chen, Xin Li, Zhang Yu, Xiong Liang, and Jiang Ma\*

The scarcity of fresh water is a pressing issue globally, and solar water evaporation technology has emerged as a leading method for producing fresh water. However, the preparation of solar evaporators is hindered by high costs, complexity, and environmental concerns. In this work, a solar evaporator with hierarchical porous structure is prepared using a simple, low-cost, and environmentally friendly dissolution manufacturing strategy. Excellent photothermal conversion capability and salt drainage performance are found owing to its hierarchical porous structure. The prepared sample exhibits a water evaporation rate of  $2.19 \text{ kg m}^{-2} \text{ h}^{-1}$  and achieves evaporation efficiency of 84.3% under one sun. Furthermore, the evaporation rates of the samples in seawater and methylene blue are 2.04, and  $1.98 \text{ kg m}^{-2} \text{ h}^{-1}$ , respectively. The evaporation rate remains stable after ten evaporation cycles. The strategy also overcomes the dimensional limitations of traditional methods, as large-size samples prepared by this strategy are successfully evaluated for evaporation experiments with natural seawater under sunny weather, and the quantity of water collected is  $\approx 170 \text{ g}$  in 6 h. The proposed strategy will offer not only sustainable water purification technologies, but also new routes for solar water evaporation, solar steam generation, and photothermal drive fields.

in many countries worldwide. Nearly one-third of the world's population,  $\approx 2$  billion people, lack access to a reliable source of safe freshwater.<sup>[1–4]</sup> Effectively solving this global challenge is of great significance for the survival and development of humankind. Given these circumstances, the development of freshwater resources has become a cutting-edge research topic, and various methods of producing freshwater are constantly being explored. Desalination technology is considered as a green solution to the worldwide freshwater shortage. The widely available desalination technologies are osmosis<sup>[5–7]</sup> and distillation.<sup>[8–10]</sup> Osmosis has a high desalination rate with high freshwater quality;<sup>[11–13]</sup> nevertheless, it requires high pretreatment of seawater, complicated procedures, and high-cost membranes. Seawater desalination systems that rely on distillation are currently experiencing rapid growth due to their exceptional efficiency and reliability. For a long time, distillation-based desalination has played a substantial role in desalination

technology. However, it encounters several challenges, including the generation of highly concentrated brine waste and the significant consumption of conventional energy resources. Additionally, the air pollution resulting from greenhouse gas emissions and other pollutants produced by conventional energy-driven desalination methods adds to the list of issues.<sup>[14,15]</sup> Consequently, the development and implementation of renewable energy sources for desalination have become imperative. These initiatives are essential for meeting society's future demands and reducing the environmental impact associated with desalination processes. This compelling necessity has driven the development of solar evaporation systems. The critical component of a solar-powered evaporation desalination system is a light absorber with broad-spectrum solar absorption performance, high photothermal conversion performance, and excellent water transport capabilities.<sup>[16–19]</sup> Currently, various photothermal materials have been widely used in solar steam generation systems, such as nanomaterials,<sup>[20–25]</sup> carbonization materials<sup>[26–30]</sup> and porous materials.<sup>[16,31–34]</sup> While nanomaterials and carbonization materials own excellent solar energy absorption, their lacking of a smooth water path prevents them from achieving a unified process of light absorption and water transportation. In contrast, porous materials play an indispensable role in the water

## 1. Introduction

The continuous expansion of industrial activities and increasing population have led to a shortage of natural freshwater resources

W. Ruan, H. Zhang, J. Huang, Z. Liu, S. Zeng, Z. Chen, Z. Yu, X. Liang, J. Ma  
State Key Laboratory of Radio Frequency Heterogeneous Integration  
Shenzhen University  
Shenzhen 518060, China  
E-mail: majiang@szu.edu.cn

J. Fu, Z. Li  
Department of Mechanics and Aerospace Engineering  
Southern University of Science and Technology  
Shenzhen 518055, China  
E-mail: fujn2022@mail.sustech.edu.cn

X. Li  
School of Mechanical  
Electrical and Information Engineering  
Shandong University  
Weihai 264209, China

 The ORCID identification number(s) for the author(s) of this article can be found under <https://doi.org/10.1002/adfm.202312314>

DOI: 10.1002/adfm.202312314

evaporation process due to their unique pore structure. Facilitating steam dispersion within pores and creating a smooth water pathway is able to aid in preventing salt accumulation on the surface, ultimately guaranteeing stable and efficient steam generation. Porous materials are regarded as the ideal materials for achieving more robust water evaporation performance.

Numerous applications of porous materials prepared with different processes for solar water evaporation have been reported, including the C-L-Wood, acquired from surface carbonization treatment of natural trees cut along the longitudinal direction.<sup>[35]</sup> A physical vapor deposition (PVD) process assisted by templates is utilized to prepare the self-assembly of gold nanoparticles on nanoporous templates,<sup>[17]</sup> a carbon foam layer is used to support an exfoliated graphite layer in a double-layer structure,<sup>[36]</sup> and by employing a one-step dealloying approach, it is possible to create a self-supporting NP–Cu film that is both highly porous and lightweight.<sup>[37]</sup> While the preparation of natural wood is simple, the structure of charred natural wood is affected, resulting in low solar evaporation efficiency. The high cost of self-assembled metallic nanoparticles is an obstacle to their large-scale applications, and the preparation of porous structures by stripping and dealloying methods displays the disadvantages of a long preparation cycle and complicated process. Therefore, the development of a simple, convenient, low-cost, and highly efficient technique for the preparation of porous materials with excellent solar evaporation rate and mass production ability has shown great potential for application in solar water evaporation.

In this work, we implemented an environmentally friendly, rapid, and cost-effective dissolution strategy called dissolution manufacturing (DM). DM involves bonding amorphous materials with soluble particulate materials, which are then dissolved in a corresponding solvent. This strategy allows for controlled preparation of porous amorphous materials by avoiding the effect of melting viscosity on pores and controlling the particle size and structure of soluble templates. By utilizing this strategy, we have designed a lightweight, adjustable shape, and flexible hierarchical porous structure (CB-HP) for solar water evaporation. Having a low overall materials cost at \$1.2 m<sup>-2</sup>. CB-HP showed a light average absorption performance of over 90%, mainly attributed to the encapsulated carbon black (CB) and hierarchical structure in its design. It exhibits superior photothermal properties under laser irradiation at wavelengths of 405, 532, 655, 808, and 1064 nm. Based on its excellent absorption performance and interconnected porous structure, CB-HP exhibits exceptional purification properties in the fields of seawater desalination and wastewater treatment. CB-HP performed outstanding solar evaporation rates in pure water, seawater, and MB solution under one sun, with the rates of 2.19, 1.98, and 2.04 kg m<sup>-2</sup> h<sup>-1</sup>, respectively. Moreover, the evaporation performance stayed relatively stable after ten cycles. Additionally, for a better test of the effect of water evaporation in the virtual environment, A large size CB-HP (23 cm × 23 cm) prepared by this strategy achieved a mass change of 5.89 kg m<sup>-2</sup> under 6 h outdoors. It also displays satisfactory water collection under different weather conditions. We believe that this simple and environmentally friendly technique possess the potential to open up new pathways for the industrial production of low-cost solar absorbers and has tremendous implication prospect for obtaining water resources in impoverished and arid regions.

## 2. Results and Discussion

### 2.1. Preparation and Characterization of CB-HP

The schematic diagram for preparing CB-HP is shown in **Figure 1a**. Polyvinylidene fluoride (PVDF) exhibits excellent flowability when heated to a suitable temperature, allowing it to fill the gaps between CB and NaCl.<sup>[38,39]</sup> After placing the resulting CB-HP with NaCl in water, the internal NaCl dissolves and creates a hierarchical porous structure. The CB-HP then demonstrates a visual effect of glossy black color. The CB-HP prepared in this way exhibits ultra-lightweight characteristics, which enable it to be effortlessly placed on rabbit tail grass (**Figure 1b**). Furthermore, CB-HP also shows a high level of shape adjustment, including the ability to easily transform into square, pentagram, and round shapes (**Figure 1c**). Even on some complex surfaces, CB-HP easily attaches to these surfaces (**Figure 1d**). The microtopography of the prepared CB-HP is presented in **Figure 1e–g**, where the surface is covered with microporosity and nano-scale pores are distributed on top of micro-scale pores, resulting in the emergence of a hierarchical porous structure. The hierarchical effect of the NaCl powder utilized in the preparation process is responsible for the formation of this structure (**Figure S1**, Supporting Information). It can be noticed that CB-HP has an integral hierarchical porous structure of interconnected orifices, with channels connecting the bottom and top layers, which plays a vital role in the regular continuous transport of water during solar water evaporation.<sup>[40]</sup> The N<sub>2</sub> adsorption and desorption curves further prove its internal porous structure (**Figure 1h**), and the specific surface area measured with the Brunauer–Emmett–Teller (BET) method is 40.9202 m<sup>2</sup> g<sup>-1</sup> for N<sub>2</sub> as a probe molecule. The nanopore distribution of CB-HP measured by BET method (**Figure S3**, Supporting Information). Fourier transform infrared spectroscopy (FTIR) is used to analyze functional groups of CB, PVDF, and CB-HP (**Figure 1i**). The peak at 1404 cm<sup>-1</sup> represents the deformation vibration absorption peak of CH<sub>2</sub> connected to CF<sub>2</sub> in PVDF, and the peaks at 976, 854, 796, and 763 cm<sup>-1</sup> represent the vibrational absorption of the crystalline phase. **Figure 1f** displays the elemental mapping image by the energy-disperse spectroscopy (EDS), which clearly shows that CB is uniformly distributed on the porous structure.

### 2.2. Photothermal Performance of CB-HP

Optical absorption plays a significant role in solar water evaporation. Optical absorption, reflection, and transmission spectra were measured to quantify the optical absorption properties of CB-HP (**Figure 2a,b**; **Figure S4**, Supporting Information). Compared to CB-HP and CB-plate, the PVDF plate has a higher transmission rate (**Figure S4**, Supporting Information). **Figure 2a,b** illustrates the absorption performance and reflection performance of CB-HP and CB-plate. The average absorption of both CB-HP and CB-plate is about 90% between 750 and 2500 nm. CB-HP exhibits higher absorption, mainly due to the hierarchical pore structure. **Figure 2c** illustrates the absorption mechanism of CB-HP, where most of the absorption is primarily caused by CB. Further absorption is enhanced due to multiple reflections of the incident light in the hierarchical pore structure. When light

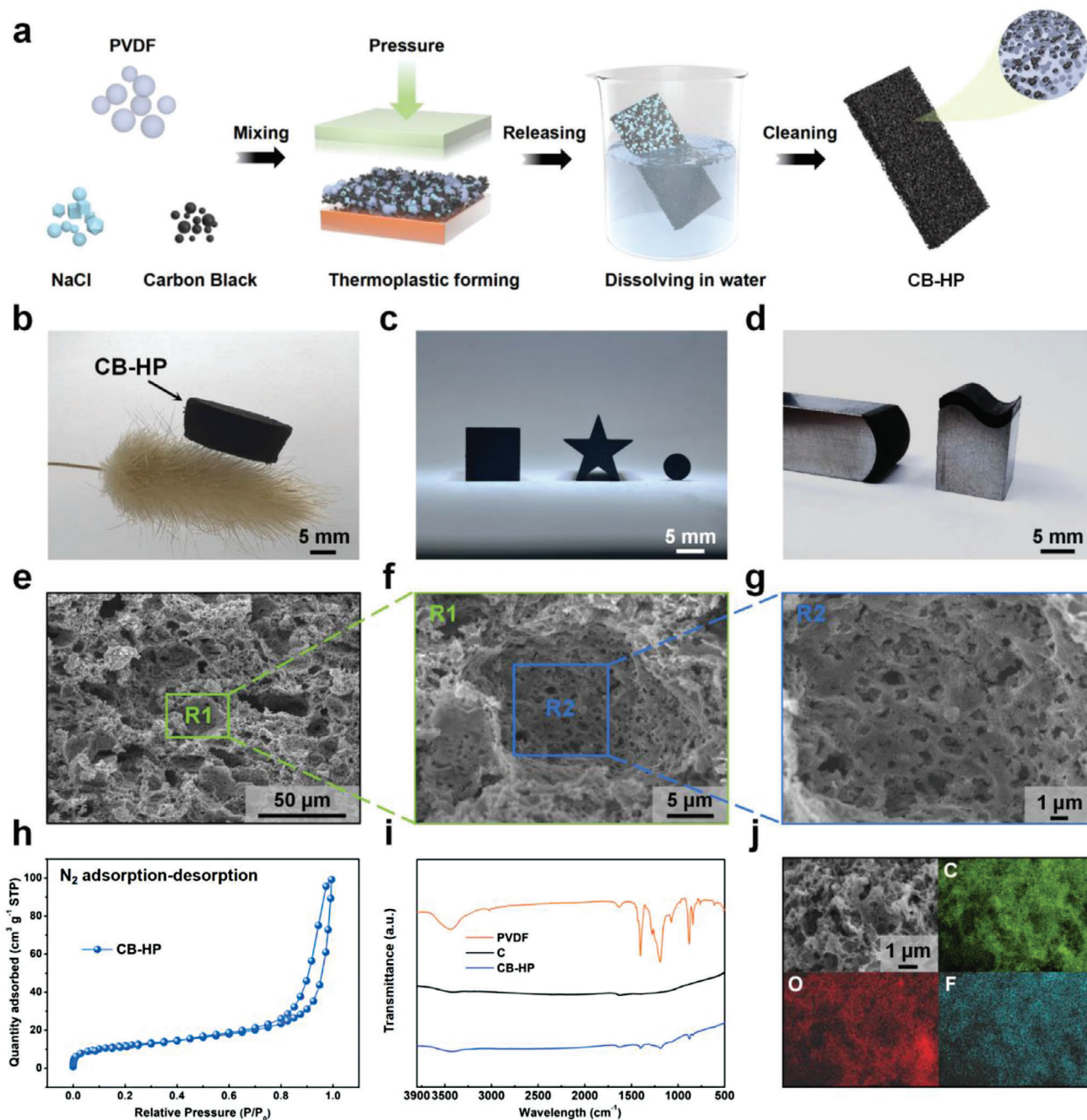


**Figure 1.** a) The schematic diagram for preparing CB-HP. b) The CB-HP is placed on rabbit tail grass. c) The photo of CB-HP in different shapes by DM strategy. d) CB-HP is attached to the curved surface. e–g) The SEM images of the micropore and nanopores on the CB-HP. h) The  $N_2$  adsorption and desorption curves of CB-HP. i) The FTIR of CB, PVDF, and CB-HP. j) The element analysis of CB-HP.

enters the structure, it is reflected back and forth multiple times, resulting in a strong suppression of reflection which improves the absorption performance of the CB-HP.<sup>[41]</sup> Based on these advantages, CB-HP exhibits outstanding absorption characteristics across the solar spectrum, indicating a promising application in the field of photothermal conversion (Figure 2d). To evaluate the photothermal performance of the CB-HP, the temperature changes on the CB-HP surface were recorded under different

power laser irradiation. Figure 2e demonstrates a positive correlation between the 808 nm laser power density and the temperature rise observed in CB-HP, which shows a temperature increase of up to  $\approx 105^\circ\text{C}$  under a laser power density of  $0.5\text{ W cm}^{-2}$  while maintaining a relatively stable and rapid response under rapid on/off conditions. Subsequently, different lasers (405, 532, 655, and 1064 nm) were used to measure the photothermal effect of CB-HP under a power density of  $0.1\text{ W cm}^{-2}$  for 1 h with each

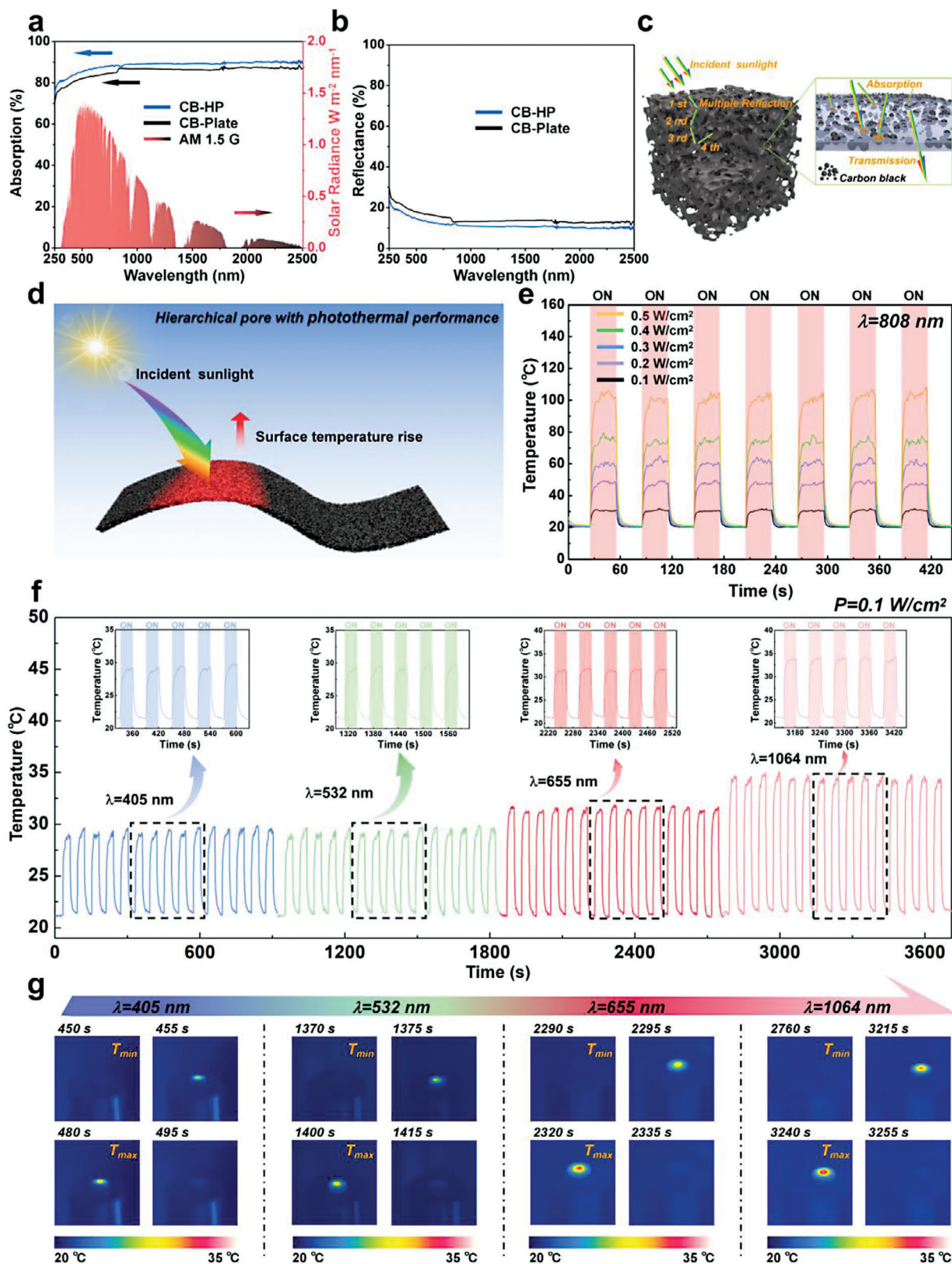


**Figure 2.** a) Absorption and b) Reflectance spectra of the CB-HP and CB-plate. c) The absorption mechanism of CB-HP. d) The photothermal conversion schematic of CB-HP. e) Temperature rise curve of CB-HP under different power irradiation with an 808 nm laser under different power densities. f) The temperature rise curve of CB-HP under different wavelength irradiation at a power density of 0.1 W cm<sup>-2</sup>. g) Infrared images of CB-HP under different wavelength irradiation at a power density of 0.1 W cm<sup>-2</sup>.

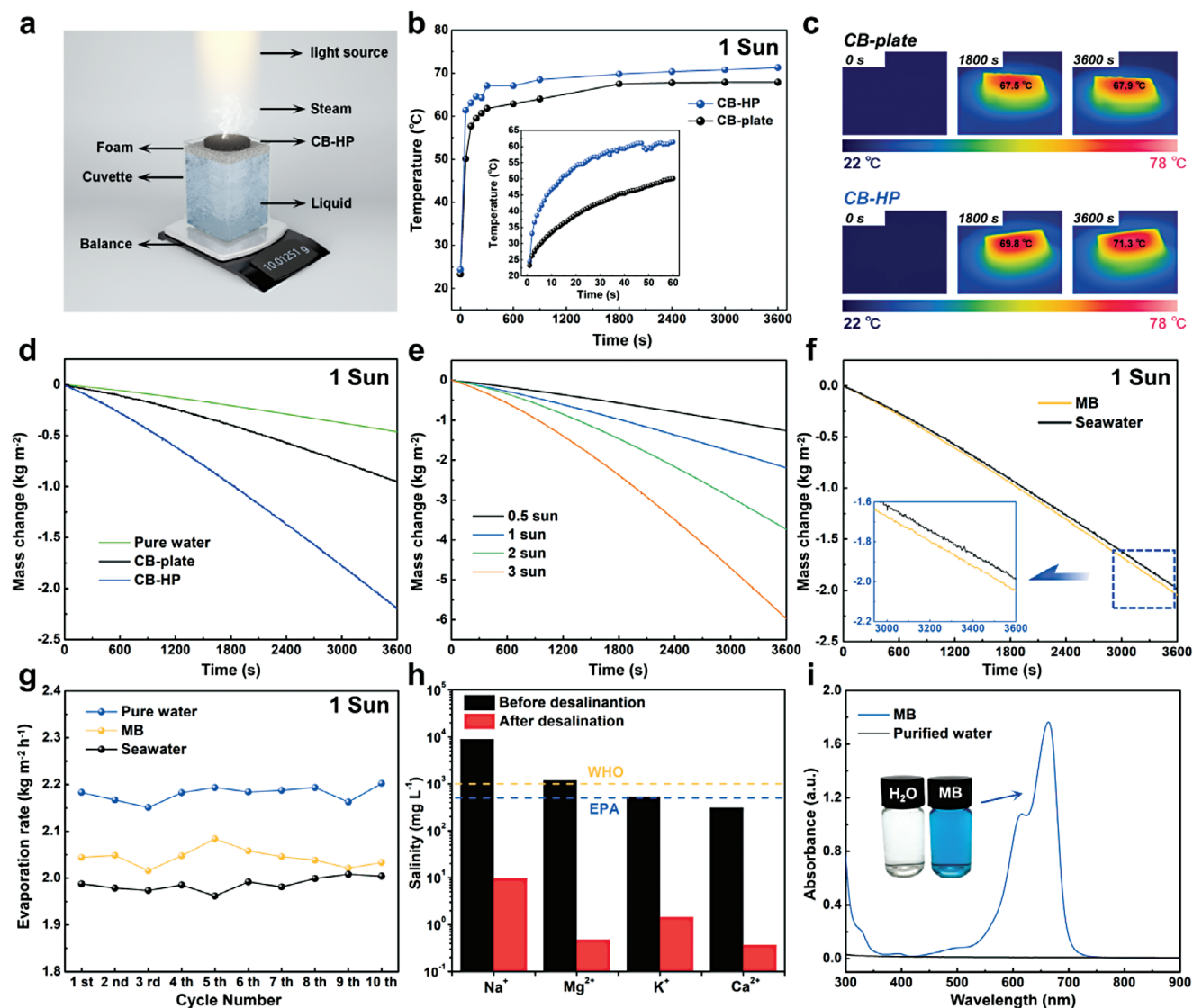


**Figure 3.** a) Schematic diagram for measuring the evaporation performance of CB-HP. b) Temperature curves of the CB-HP and CB-plate under one sun solar irradiation, the inset is an enlarged view of the first 60 s. c) The temperature distribution infrared images of CB-HP and CB-plate under one sun solar irradiation. d) Mass change of water over time of CB-HP, CB-plate, and pure water under one sun solar irradiation. e) Mass change of water over time for the CB-HP under different sun irradiation. f) Mass change of seawater and MB over time of CB-HP in pure water, seawater, and MB under one solar irradiation for ten cycles. g) Stability of CB-HP in pure water, seawater, and MB under one solar irradiation for ten cycles. h) The concentrations of  $\text{Na}^+$ ,  $\text{Mg}^{2+}$ ,  $\text{K}^+$ , and  $\text{Ca}^{2+}$  in actual seawater samples (Huanghai Sea) before and after desalination, the dashed line represents the WHO and EPA standards. i) UV-vis-NIR absorption spectra of seawater and evaporated water before and after evaporation of seawater by CB-HP.

laser. The temperature curve of CB-HP was recorded in Figure 2f, and the corresponding infrared image is shown in Figure 2g. Remarkably, CB-HP also exhibits rapid surface temperature elevation within just 5 s under irradiation with different laser wavelengths and retains this performance without significant loss even after 15 consecutive cycles. As mentioned previously, CB-HP displays favorable photothermal conversion performance at wavelengths of 405, 532, 655, and 1064 nm while also demonstrating excellent cycling stability. These characteristics will enable CB-HP to have application prospects in some photothermal fields, such as photothermal drive, solar water evaporation, photothermal imaging, etc.

### 2.3. Evaporation Performance of CB-HP

Based on the photothermal performance and interconnected porous structure of CB-HP, a series of experimental evaluations were conducted to assess its solar evaporation performance. Figure 3a shows the schematic diagram of CB-HP for solar water evaporation, which mainly includes a glass container for water, a CB-HP based solar absorber, and an electronic balance. The CB-HP was embedded in the sinkhole of the foam, and the water in the foam penetrated onto the CB-HP surface from the bottom as well as the side. Additionally, considering that the water absorbed in the foam will also evaporate under the sunlight, to

prevent the water from being heated and to ensure the measurement accuracy of the evaporation process, all parts of the foam except for the CB-HP were wrapped with tinfoil to ensure that only the surface of the CB-HP was exposed to the sunlight. The physical diagram of the experimental setup can be seen in Figure S5 (Supporting Information). Different from the photothermal effect when a single-wavelength laser irradiates CB-HP, the temperature changes of CB-HP under simulated sunlight ( $1 \text{ kW m}^{-2}$ ) were evaluated and shown in Figure 3b. The infrared image records the temperature distribution of the CB-HP, CB-plate, and PVDF at a certain moment (Figure 3c; Figure S7, Supporting Information). The temperature rise curves of CB-HP, CB-plate, and PVDF under one sun solar irradiation were collected (Figure 3b; Figure S6, Supporting Information). It can be seen very obviously that the temperature of CB-HP is significantly higher than that of CB-plate. Within five minutes of irradiation, the temperatures of both CB-HP and CB-plate increased rapidly and stabilized after twenty minutes. The temperature of CB-HP, CB-plate, and PVDF increased to 71.3, 67.9, and 32.8 °C under one sun irradiation, respectively.

Subsequently, the evaporation rates of CB-HP, CB-plate, and pure water were measured (Figure 3d). CB-HP has a higher evaporation rate of  $2.19 \text{ kg m}^{-2} \text{ h}^{-1}$ , which is 2.3 times higher than that of CB-plate and 4.8 times higher than that of pure water. The CB-HP exhibits an evaporation rate of  $1.78 \text{ kg m}^{-2} \text{ h}^{-1}$  even the dark evaporation rate is removed (Figure S8, Supporting Information). Accordingly, the solar-vapor evaporation efficiency,  $\eta$ , can be defined as<sup>[42]</sup>

$$\eta = \alpha - \eta_{\text{Rad}}, N - \eta_{\text{Conv}}, N - \eta_{\text{Cond}}, N \quad (1)$$

$\eta$  is the evaporation efficiency,  $\eta_{\text{Rad}}$  shows the radiation loss,  $\eta_{\text{Conv}}$  represents the convection loss, and  $\eta_{\text{Cond}}$  is the conduction loss. Details of the calculation are given in Note S1.

For testing the stability performance of CB-HP under different solar power irradiation, water evaporation experiments were conducted at half sun, one sun, two suns, and three suns (Figure 3e), and it is clearly seen that the evaporation rate increases with power density, and the evaporation curve shape remains smooth without sudden fluctuations. Due to the uneven distribution of water resources worldwide, with the vast majority of water resources being occupied by seawater, and water pollution caused by energy development, the application of CB-HP for desalination and purification of wastewater is of great significance in solving real-world scarcity of water resources.<sup>[43,44]</sup> Therefore, the performance of CB-HP in desalination of seawater and purification of wastewater was evaluated. Using natural seawater in the Yellow Sea of China and simulated wastewater using MB as a dye, both the seawater and the MB solutions had satisfactory evaporation rates under one sun (Figure 3f), with evaporation rates being  $2.04$  and  $1.98 \text{ kg m}^{-2} \text{ h}^{-1}$ , respectively. To check the reusability of CB-HP, ten cycles of CB-HP were irradiated in pure water, seawater, and MB, respectively. It can be clearly seen that the evaporation rate of CB-HP fluctuates only within a small range during ten cycles of solar irradiation, and CB-HP has excellent evaporation stability (Figure 3g). Additionally, the concentrations of  $\text{Na}^+$ ,  $\text{Mg}^{2+}$ ,  $\text{K}^+$ , and  $\text{Ca}^{2+}$  ions in seawater and evaporated collected water were also measured. They meet the drinking water standards specified by the World Health Organization (WHO)

and the United States Environmental Protection Agency (EPA) (Figure 3h). UV-vis-NIR absorption spectra (Figure 3i) of MB solutions before and after evaporation were measured by UV spectrophotometer (UV1280). There is a strong absorption peak at 660 nm before MB evaporation, while the absorption peak of the water collected after evaporation from the CB-HP disappears, indicating the complete purification of the MB. The inset graph also shows that the original blue solution becomes colorless. The superior evaporation performance and cyclic stability of CB-HP have great potential for desalination and wastewater treatment applications.

In order to demonstrate the superiority of our prepared solar water evaporation porous materials, we have summarized the evaporation performance of solar water evaporation materials in previous studies (Figure 4; Table S1, Supporting Information). The porous carbon with a well-defined structure was prepared by controlled carbonization of biomass/waste plastic using eutectic salts to achieve 82.6% evaporation efficiency and  $1.7 \text{ kg m}^{-2} \text{ h}^{-1}$  evaporation rate.<sup>[45]</sup> The foldable graphene film had an evaporation rate of  $1.45 \text{ kg m}^{-2} \text{ h}^{-1}$  and an evaporation efficiency of 80%.<sup>[46]</sup> The 2D MXene had an evaporation rate of  $1.31 \text{ kg m}^{-2} \text{ h}^{-1}$  and an evaporation efficiency of 71%.<sup>[47]</sup> Among the numerous materials, our material exhibits remarkable evaporation rates and satisfactory evaporation efficiencies. In addition, we also summarized the cost and process time of materials in previous studies (Figure S9, Table S2, Supporting Information). In the realm of materials used for the production of solar evaporators, various options exist, each with its associated cost. For instance, hybrid hydrogel evaporators (HEEs) present a total materials cost of  $\approx \$14.9$  per square meter.<sup>[48]</sup> Another alternative is nanofilms based on polypyrrole (PPy) coated stainless steel (SS) mesh, which comes at a cost of around  $\$55$  per square meter.<sup>[49]</sup> The lotus leaf like vertical hierarchical solar vapor generator (LSG) assembled from Si/PPy-PVA sponge and multiple columns of PVA sponge cost  $\$13.86$  per square meter.<sup>[50]</sup> The emergence of the CB-HP solar evaporator represents a breakthrough in this field. This technology stands out by offering remarkable advantages. The CB-HP is outstanding in cost-effectiveness and manufacturing process compared to most of the materials currently. The innovative CB-HP approach enables the production of samples within just 1 h and does so at an impressively low cost of only  $\$1.2$  per square meter.

Excellent desalination performance is pivotal to achieving continuous, stable, and high evaporation efficiency in the solar evaporator. The porous structure is significant for smooth water transport and hinders salt accumulation.<sup>[37]</sup> The water transport capacity of the sample can be measured by testing the speed of water infiltration into the sample. The speed of water penetration into the sample can be reflected by wettability. Figure 5a depicts when a drop of water is applied to the surface of the CB-HP and CB-plate. After contacting the CB-HP surface, the water droplets are completely absorbed after 3 s. In contrast, the water contact angle of CB-plate ranged from 128° to 125° after 3 s (Figure 5b). In addition, salt accumulation on the material pores may cause a decrease in the evaporation efficiency. Therefore, we evaluated the salt removal capacity of CB-HP. A layer of salt was placed on the upper surface of the CB-HP to simulate salt accumulation on the surface of the sample during evaporation (Figure 5c). Within a minute, the apparent water distribution can be seen

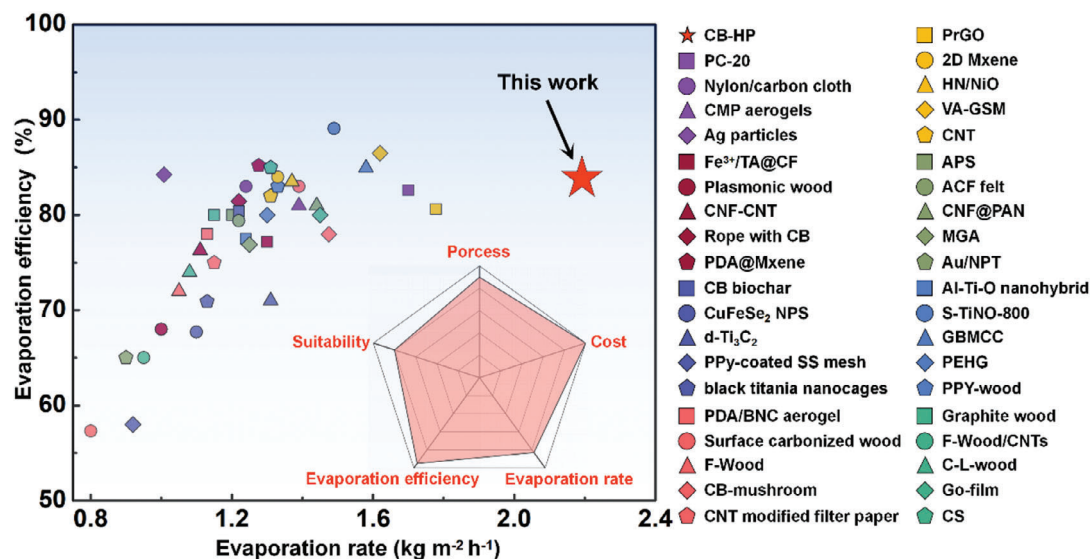


Figure 4. The comparison of the evaporation efficiency and evaporation rate of the previous materials.

on the surface of CB-HP. After 30 min, most of the salt was removed from the CB-HP surface. To clearly express this process, Figure 5d schematically presents the salt and water transport process. The interconnected porous pathways transport water to the upper surface, gradually carrying the salt away without blocking the pathways. These characteristics are indispensable in enhancing the evaporation rate and stability of CB-HP in the evaporation process.

Furthermore, our process has successfully produced large-sized CB-HP with sufficient strength to be held by hand (Figure 6a). The CB-HP was able to float on the surface of seawater, demonstrating its effectiveness. To further evaluate its functional performance under realistic conditions, we conducted an outdoor solar desalination experiment in natural sunlight, using a  $23 \times 23$  cm CB-HP and a glass plate as the solar absorber. Real-time recordings were taken of the solar power, temperature, and mass change throughout the day (Figure 6b). The mass change of water was monitored over a 6-h period (10:30–16:30, 28 April 2023, Shenzhen, China) and showed continuous evaporation (Figure 6c). This indicates that water was being continuously evaporated. Then, the stability of the large-size CB-HP was measured under different weather conditions, and the results are shown in Figure 6d. The device collected 170 g of water in 6 h of clear weather, 106 g in cloudy weather, and 70 g even in overcast days. After ten days of collection testing, CB-HP demonstrated stable evaporation collection in the natural environment. The electrical resistance of seawater, collected evaporated seawater, and distilled water was tested, which showed that the resistance of collected evaporated seawater had a significant reduction compared to the original seawater resistance and tended to be similar to the distilled water resistance (Figure S10, Supporting Information). This verifies that the collected water after CB-HP evaporation fulfills the freshwater intake requirements for humans. Additionally, the required size and shape of CB-HP can be easily customized with a simple process and low cost, demonstrating its promising application in the development of large-scale solar evaporators.

### 3. Conclusion

We implemented an environmentally friendly, rapid, and cost-effective DM strategy to prepare the CB-HP by mixing CB, PVDF, and NaCl. CB-HP has excellent photothermal conversion performance and hydrophilicity. These performances enable CB-HP to exhibit an evaporation rate of  $2.19 \text{ kg m}^{-2} \text{ h}^{-1}$  under  $1 \text{ kW m}^{-3}$  and achieve an evaporative efficiency of 84.3%. We also verified its salt drainage capacity and water quality and showed that CB-HP could produce fresh water that meets the human intake requirements with a simple process and low cost. Moreover, the size and shape of CB-HP can be customized according to our needs by DM strategy. This study suggests that CB-HP is a promising material for the development of large-scale solar evaporators that can address the global water scarcity problem. Further research is needed to optimize the design and performance of CB-HP and explore its applications in other fields, such as electromagnetic shielding, sensing, filtering, etc.

### 4. Experimental Section

**Materials:** Given the versatility of PVDF in various fields and its advantageous properties, such as low processing temperature, easy molding, and low cost. PVDF polymer was chosen as the linker for the study. PVDF powder with a particle size of  $\approx 5 \mu\text{m}$  were purchased from Huachuang Plastic Chemical Co. Ltd in Dongguan and CB powder with a particle size of  $\approx 20 \text{ nm}$ , and NaCl were purchased from Maclean Biochemical Technology Co. Ltd in Shanghai. The NaCl powder needs to be recrystallized and ball-milled to prepare the size of  $\approx 700 \text{ nm}$ .

**Preparation of CB-HP:** The prepared NaCl powder, CB and PVDF were mixed in a grinding bowl with a mass ratio of 28:2:1. The homogeneously mixed powder was placed into the mold cavity and then fed into a heating chamber with a vacuum of  $3 \times 10^{-3} \text{ Pa}$ . At a temperature of  $\approx 443 \text{ K}$ , a pressure of 130 MPa was applied, and the heating and pressure were removed when the temperature reached 543 K. When the temperature was lowered to 453 K, the sample was removed from the heating device. The sample was then placed in deionized water for 2 h to dissolve the NaCl in the sample. The sample was repeatedly washed with distilled

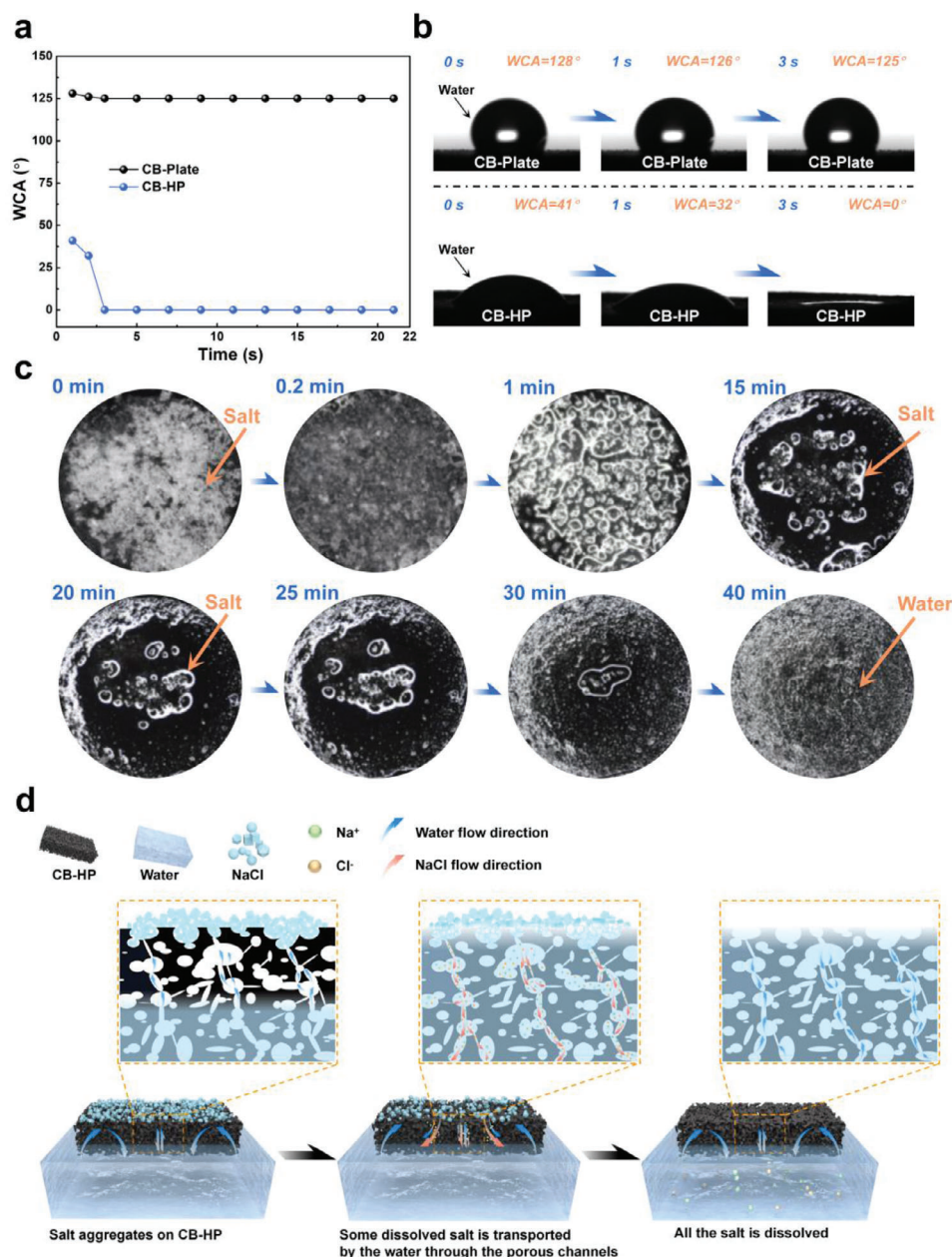


**Figure 5.** a) The relationship between contact angles of CB-HP and CB-plate with time. b) The evolution of water angle on CB-HP and the CB-plate at the initial stage. c) Optical photograph of CB-HP surface simulating dissolution changes of accumulated salt. d) Schematic diagram of the transport processes of salt and water.

water to obtain CB-HP for subsequent experiments after dissolution. CB-plate was prepared by the same process (CB and PVDF in a mass ratio of 2:1)

**Multi-Scale Characterization:** The nitrogen adsorption/desorption analysis at 77 K using a Micromeritics ASAP 2020 was conducted to calculate the specific surface area of the samples using the BET method. Differential scanning calorimetry (DSC; Perkin-Elmer DSC-8000) with a cooling/heating rate of  $20 \text{ K min}^{-1}$  was used to ascertain the melting temperature ( $T_m$ ) of the PVDF. The test results are shown in Figure S2 (Supporting Information) for serving the selection of thermoplastic forming temperatures. The morphology of CB-HP was observed using a scanning electron microscope (SEM; Fei quanta FEG 450). FTIR spectrum tested by an equip-

ment of Nicolet iN10. Transmission ( $T$ ), reflectance ( $R$ ) and absorbance ( $A$ ) were measured using UV-vis-NIR (Shimadzu UV-3600) spectrophotometer equipped with an integrating sphere. The temperature of CB-HP and CB-Plate were measured by using an infrared thermal imager (Fotric 280d). The concentrations of  $\text{Na}^+$ ,  $\text{K}^+$ ,  $\text{Ca}^{2+}$  and  $\text{Mg}^{2+}$  in the samples were collected by inductively coupled plasma atomic emission spectrometry (ICP-OES). The absorbance spectrum (from 300 to 900 nm) of dye MB and condensate was measured with a UV-vis-NIR spectrophotometer (Shimadzu UV-1280). The SEM with EDS was used to detect the element distribution of the samples. The contact angle (CA) of the microstructure surface was measured using a droplet shape analyzer (DSA100S, Krüss, Germany) with a  $1 \mu\text{L}$  water droplet volume.

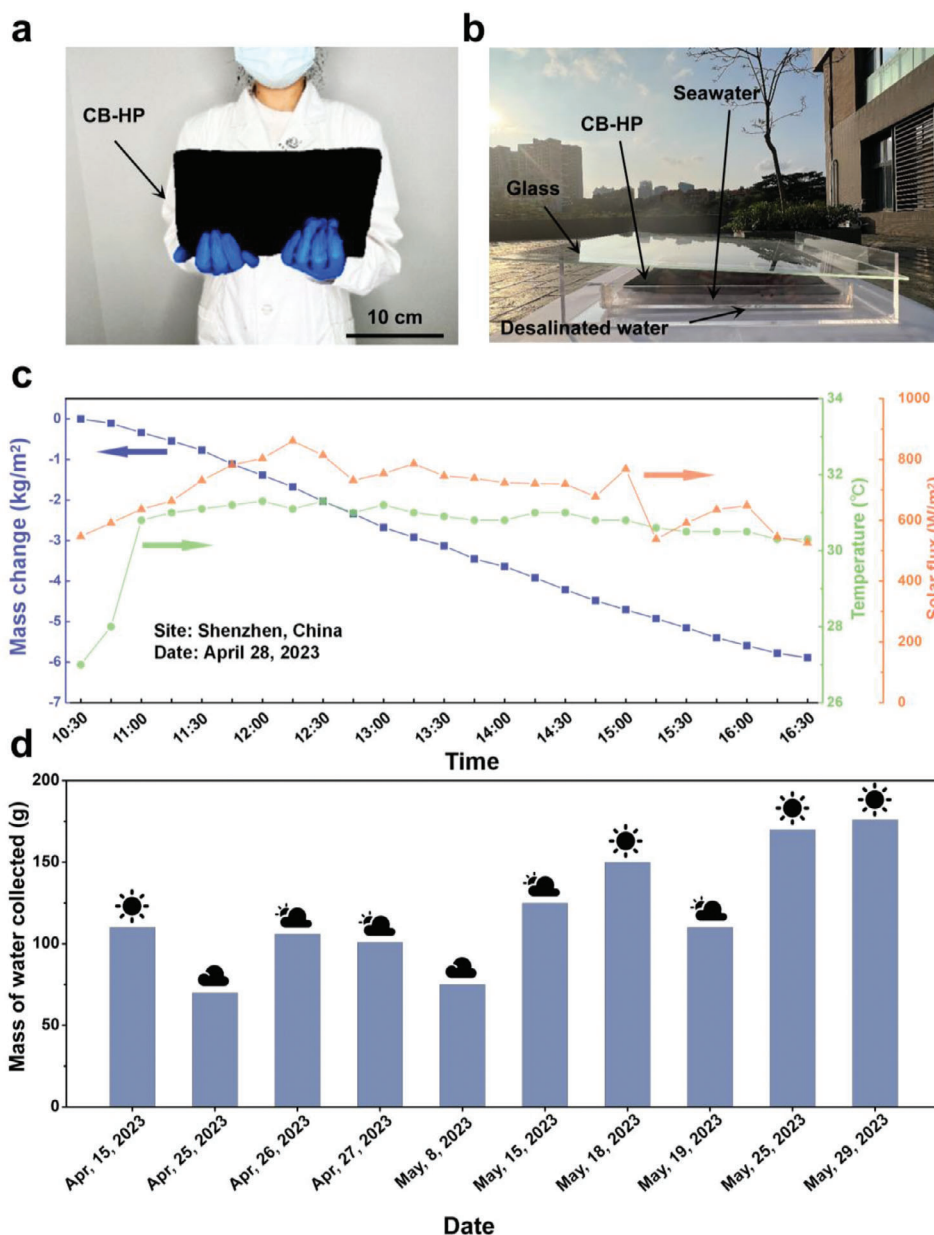


**Figure 6.** a) Optical photograph of a large CB-HP (23 × 23 cm). b) The physical device for collecting evaporated water. c) 6 h (10:30 am to 4:30 pm) (28 April 2023, Shenzhen, China) continuous measurement of the solar flux and clean water change using a large-scale CB-HP. The ambient solar flux (orange line), mass change of the water (blue line), and temperature change (green line). d) Collection of evaporated water statistics under different weather.

**The Photothermal Characterization:** To evaluate the photothermal conversion performance of CB-HP, the CB-HP placed on quartz is irradiated by 808 nm laser beams of varying power densities while the temperature change is recorded using an infrared camera. The photothermal performance of CB-HP were described using lasers of different wavelengths, namely 405 nm (PGL-V-H-405), 532 nm (PGL-V-H-532), 655 nm (PGL-V-H-655), 808 nm (5 W, fiber-tailed, multimode diode laser), and 1064 nm (PGL-V-H-1064) lasers. The sample was placed on quartz with a laser switching cycle of 60 s. The sample was then irradiated vertically for 900 s using each laser, with all four lasers being applied for a total of 3600 s. During this process, the thermal response of the surface was monitored using an infrared imaging camera at a data acquisition frequency of 1 Hz.

**Water Evaporation Characterization:** A Xe light (CEL-HXF 300, Beijing Education Au-light Co., Ltd.) with an AM 1.5 filter was set at the top of the samples to simulate the sunlight. The light intensity was monitored by a strong light power meter (CEL-NP2000, Beijing Education Au-light Co., Ltd.). The temperature was measured using an infrared thermal imager, and the mass of evaporation loss of samples was measured using an electronic balance (Sartorius Quintix35-1CN, measurement accuracy (0.01 mg) connected to a computer. The computer that records the change of the value of the electronic balance in real time, when the CB-HP is embedded in the sink hole of the foam, the water in the foam penetrates to the surface of the CB-HP from the bottom as well as the side, and then turn on A Xe light to adjusting its power to 1 sun. Pure water is

evaporated in the form of vapor, resulting in a reduction in the mass change of water in the glass bottle. In addition, considering that the water absorbed in the foam will also evaporate under the sunlight, in order to ensure the measurement accuracy of the evaporation process, the glass bottle and the foam except the sample are wrapped with tinfoil to ensure that only the surface of the sample is exposed to the sunlight.

**The Outdoor Water Evaporation Characterization:** To evaluate the performance of CB-HP under different environmental factors such as sunlight intensity and angle of incidence, a 6 h (10:30–16:30, 28 April 2023, Shenzhen, China) outdoor experiment using CB-HP (Length and width sizes are 23 × 23 cm) under natural sunlight was conducted. The environmental temperature was measured using an infrared thermal imager. The sunlight intensity was monitored by a strong light power meter (CEL-NP2000, Beijing Education Au-light Co.). The mass of evaporation loss of samples was measured using an electronic balance with a measurement accuracy of 0.1 g.

## Supporting Information

Supporting Information is available from the Wiley Online Library or from the author.

## Acknowledgements

The work was financially supported by the Key Basic and Applied Research Program of Guangdong Province, China (Grant No. 2019B030302010), the National Key Research and Development Program of China (Grant No. 2018YFA0703605), the National Science Foundation of China (Grant No. 52122105, 51971150, 52271150), and the Science and Technology Innovation Commission Shenzhen (Grants No. RCJC20221008092730037, 20220804091920001). The authors also thank the assistance on microscope observation received from the Electron Microscope Center of Shenzhen University.

## Conflict of Interest

The authors declare no conflict of interest.

## Author Contributions

W.Q.R. and H.T.Z. contributed equally to this work. J.M., W.Q.R., and J.N.F. conceived the idea, W.Q.R., X.L., and J.N.F. monitored the work, Z.Li, Z.Liu, and J.H. designed experimental steps. W.Q.R., H.T.Z. and J.N.F. completed the data analysis. X.L. and Z.C. performed the raw material preparation and SEM. W.Q.R., H.T.Z., and J.N.F. wrote the manuscript. J.M. reviewed and revised the manuscript. All authors contributed to the discussion and analysis of the results.

## Data Availability Statement

Research data are not shared.

## Keywords

dissolution manufacturing, large-size solar evaporator, photothermal conversion, porous structure, solar evaporator

Received: October 8, 2023  
Revised: November 2, 2023  
Published online:

- [1] J. Bundschuh, M. Kaczmarczyk, N. Ghaffour, B. Tomaszewska, *Desalination* **2021**, *508*, 115035.
- [2] G. Cao, Q. Li, R. Wang, C. Wang, X. Duan, S.-H. Ho, *Chem. Eng. J.* **2020**, *393*, 124750.
- [3] J. B. Zimmerman, J. R. Mihelcic, J. Smith, *Environ. Sci. Technol.* **2008**, *42*, 4247.
- [4] J. Li, N. Wang, F. Bi, S. Chen, C. Zhao, L. Liu, Q. Yao, C. Huang, Y. Xue, H. Liu, T. Jiu, *Sol. RRL* **2019**, *3*, 1800206.
- [5] A. Pugsley, A. Zacharopoulos, J. D. Mondol, M. Smyth, *Renew. Energ.* **2016**, *88*, 200.
- [6] H. Garelick, A. Dybowska, E. Valsami-Jones, N. Priest, *J. Soil. Sediment.* **2005**, *5*, 182.
- [7] C. Fritzmann, J. Löwenberg, T. Wintgens, T. Melin, *Desalination* **2007**, *216*, 1.
- [8] A. D. Khawaji, I. K. Kutubkhanah, J.-M. Wie, *Desalination* **2008**, *221*, 47.
- [9] M. A. Sharaf, A. S. Nafey, L. García-Rodríguez, *Energy* **2011**, *36*, 2753.
- [10] D. Zhao, J. Xue, S. Li, H. Sun, Q.-D. Zhang, *Desalination* **2011**, *273*, 292.
- [11] M. Elimelech, W. A. Phillip, *Science* **2011**, *333*, 712.
- [12] L. F. Greenlee, D. F. Lawler, B. D. Freeman, B. Marrot, P. Moulin, *Water. Res.* **2009**, *43*, 2317.
- [13] M. Qasim, M. Badrelzaman, N. N. Darwish, N. A. Darwish, N. Hilal, *Desalination* **2019**, *459*, 59.
- [14] F. Zhao, Y. Guo, X. Zhou, W. Shi, G. Yu, *Nat. Rev. Mater.* **2020**, *5*, 388.
- [15] K. Elsaid, M. Kamil, E. T. Sayed, M. A. Abdelkareem, T. Wilberforce, A. Olabi, *Sci. Total Environ.* **2020**, *748*, 141528.
- [16] J. Fu, Z. Li, X. Li, F. Sun, L. Li, H. Li, J. Zhao, J. Ma, *Nano. Energy.* **2023**, *106*, 108019.
- [17] L. Zhou, Y. Tan, D. Ji, B. Zhu, P. Zhang, J. Xu, Q. Gan, Z. Yu, J. Zhu, *Sci. Adv.* **2016**, *2*, 1501227.
- [18] H. Ren, M. Tang, B. Guan, K. Wang, J. Yang, F. Wang, M. Wang, J. Shan, Z. Chen, D. Wei, H. Peng, Z. Liu, *Adv. Mater.* **2017**, *29*, 1702590.
- [19] P. Mu, Z. Zhang, W. Bai, J. He, H. Sun, Z. Zhu, W. Liang, A. Li, *Adv. Energy. Mater.* **2019**, *9*, 1802158.
- [20] M. Gao, P. K. N. Connor, G. W. Ho, *Adv. Energy. Mater.* **2016**, *9*, 3151.
- [21] Y. Yang, X. Yang, L. Fu, M. Zou, A. Cao, Y. Du, Q. Yuan, C.-H. Yan, *ACS. Energy. Lett.* **2018**, *3*, 1165.
- [22] M. Zhu, Y. Li, F. Chen, X. Zhu, J. Dai, Y. Li, Z. Yang, X. Yan, J. Song, Y. Wang, E. Hitz, W. Luo, M. Lu, B. Yang, L. Hu, *Adv. Energy. Mater.* **2018**, *8*, 1701028.
- [23] K. Bae, G. Kang, S. K. Cho, W. Park, K. Kim, W. J. Padilla, *Nat. Commun.* **2015**, *6*, 10103.
- [24] Y. Liu, S. Yu, R. Feng, A. Bernard, Y. Liu, Y. Zhang, H. Duan, W. Shang, P. Tao, C. Song, T. Deng, *Adv. Mater.* **2015**, *27*, 2768.
- [25] L. Zhang, J. Xing, X. Wen, J. Chai, S. Wang, Q. Xiong, *Nanoscale* **2017**, *9*, 12843.
- [26] Y. Chen, C. Sha, Y. Yu, W. Wang, Scalable, *Adv. Sustain. Syst.* **2022**, *6*, 2100300.
- [27] J. Fang, J. Liu, J. Gu, Q. Liu, W. Zhang, H. Su, D. Zhang, *Chem. Mater.* **2018**, *30*, 6217.
- [28] X. Han, W. Wang, K. Zuo, L. Chen, L. Yuan, J. Liang, Q. Li, P. M. Ajayan, Y. Zhao, J. Lou, *Nano. Energy.* **2019**, *60*, 567.
- [29] N. Liu, L. Hao, B. Zhang, R. Niu, J. Gong, T. Tang, *Energy. Environ. Mater.* **2021**, *5*, 617.
- [30] M. Zhu, J. Yu, C. Ma, C. Zhang, D. Wu, H. Zhu, *Sol. Energ. Mat. Sol. C.* **2019**, *191*, 83.
- [31] S. He, C. Chen, Y. Kuang, R. Mi, Y. Liu, Y. Pei, W. Kong, W. Gan, H. Xie, E. Hitz, C. Jia, X. Chen, A. Gong, J. Liao, J. Li, Z. J. Ren, B. Yang, S. Das, L. Hu, *Energy Environ. Sci.* **2019**, *12*, 1558.
- [32] W. Zhao, H. Gong, Y. Song, B. Li, N. Xu, X. Min, G. Liu, B. Zhu, L. Zhou, X.-X. Zhang, J. Zhu, *Adv. Funct. Mater.* **2021**, *31*, 2100025.

- [33] X. Hu, W. Xu, L. Zhou, Y. Tan, Y. Wang, S. Zhu, J. Zhu, *Adv. Mater.* **2017**, *29*, 1604031.
- [34] P. Zhang, J. Li, L. Lv, Y. Zhao, L. Qu, *ACS. Nano.* **2017**, *11*, 5087.
- [35] H. Liu, C. Chen, G. Chen, Y. Kuang, X. Zhao, J. Song, C. Jia, X. Xu, E. Hitz, H. Xie, S. Wang, F. Jiang, T. Li, Y. Li, A. Gong, R. Yang, S. Das, L. Hu, *Adv. Energy Mater.* **2018**, *8*, 1701616.
- [36] H. Ghasemi, G. Ni, A. M. Marconnet, J. Loomis, S. Yerci, N. Miljkovic, G. Chen, *Nat. Commun.* **2014**, *5*, 4449.
- [37] B. Yu, Y. Wang, Y. Zhang, Z. Zhang, *Nano-Micro. Lett.* **2023**, *15*, 94.
- [38] X. Ren, N. Meng, H. Zhang, J. Wu, I. Abrahams, H. Yan, E. Bilotti, M. J. Reece, *Nano. Energy.* **2020**, *72*, 104662.
- [39] N. Meng, X. Ren, G. Santagiuliana, L. Ventura, H. Zhang, J. Wu, H. Yan, M. J. Reece, E. Bilotti, *Nat. Commun.* **2019**, *10*, 4535.
- [40] X. P. Li, X. Li, H. Li, Y. Zhao, J. Wu, S. Yan, Z. Z. Yu, *Adv. Funct. Mater.* **2022**, *32*, 2110636.
- [41] K. Li, T.-H. Chang, Z. Li, H. Yang, F. Fu, T. Li, J. S. Ho, P.-Y. Chen, *Adv. Energy Mater.* **2019**, *9*, 1901687.
- [42] X. Fan, Y. Yang, X. Shi, Y. Liu, H. Li, J. Liang, Y. Chen, *Adv. Funct. Mater.* **2020**, *30*, 2007110.
- [43] L. Zhou, Y. Tan, J. Wang, W. Xu, Y. Yuan, W. Cai, S. Zhu, J. Zhu, *Nat. Photonics.* **2016**, *10*, 393.
- [44] W. Xu, X. Hu, S. Zhuang, Y. Wang, X. Li, L. Zhou, S. Zhu, J. Zhu, *Adv. Energy Mater.* **2018**, *8*, 1702884.
- [45] L. Hao, N. Liu, R. Niu, J. Gong, T. Tang, *Sci. China. Mater.* **2021**, *65*, 201.
- [46] X. Li, W. Xu, M. Tang, L. Zhou, B. Zhu, S. Zhu, J. Zhu, *Proc. Natl. Acad. Sci. USA.* **2016**, *113*, 13953.
- [47] J. Zhao, Y. Yang, C. Yang, Y. Tian, Y. Han, J. Liu, X. Yin, W. Que, *J. Mater. Chem. A.* **2018**, *6*, 16196.
- [48] Y. Guo, H. Lu, F. Zhao, X. Zhou, W. Shi, G. Yu, *Adv. Mater.* **2020**, *32*, 1907061.
- [49] L. Zhang, B. Tang, J. Wu, R. Li, P. Wang, *Adv. Mater.* **2015**, *27*, 4889.
- [50] S. Cheng, Z. Yu, Z. Lin, L. Li, Y. Li, Z. Mao, *Chem. Eng. J.* **2020**, *401*, 126108.